

Monte Carlo modeling of thin GaAs photocathodes

Cite as: J. Appl. Phys. **126**, 075706 (2019); <https://doi.org/10.1063/1.5113804>

Submitted: 07 June 2019 . Accepted: 23 July 2019 . Published Online: 19 August 2019

Wei Liu , and Erdong Wang 



View Online



Export Citation



CrossMark

ARTICLES YOU MAY BE INTERESTED IN

[Effect of illumination on the interplay between Dresselhaus and Rashba spin-orbit couplings in InAs quantum wells](#)

Journal of Applied Physics **126**, 075704 (2019); <https://doi.org/10.1063/1.5110476>

[Design of selector-based insulator-metal transition model for TiO₂ bipolar resistive random access memory](#)

Journal of Applied Physics **126**, 075705 (2019); <https://doi.org/10.1063/1.5099953>

[Focused acoustic vortex by an artificial structure with two sets of discrete Archimedean spiral slits](#)

Applied Physics Letters **115**, 083501 (2019); <https://doi.org/10.1063/1.5108687>

Journal of
Applied Physics

SPECIAL TOPIC:
Polymer-Grafted Nanoparticles

Submit Today!

Monte Carlo modeling of thin GaAs photocathodes

Cite as: J. Appl. Phys. **126**, 075706 (2019); doi: [10.1063/1.5113804](https://doi.org/10.1063/1.5113804)

Submitted: 7 June 2019 · Accepted: 23 July 2019 ·

Published Online: 19 August 2019



Wei Liu  and Erdong Wang 

AFFILIATIONS

Brookhaven National Laboratory, Upton, New York 11973, USA

^{a)}Electronic mail: wange@bnl.gov

ABSTRACT

A Monte Carlo model was developed to simulate electron transport and emission from thin GaAs photocathodes with different active layer thicknesses and dopant concentrations. The simulation accurately predicts expected behavior, namely, quantum efficiency (QE) is enhanced for thicker GaAs photocathodes and for higher dopant concentrations. More significantly, the simulation predicts that electrons excited to the conduction band of the GaAs can be reflected by the band bending regions of the AlGaAs barrier layer, which contributes to enhance QE. The simulation also predicts that electrons in the conduction band suffer more scattering for thicker GaAs photocathodes and for higher dopant concentration, leading to longer emission response time. This Monte Carlo model will improve our understanding and predicting of the performance of more complicated GaAs-based heterojunction structures composed of multiple thin layers.

Published under license by AIP Publishing. <https://doi.org/10.1063/1.5113804>

I. INTRODUCTION

GaAs-based photocathodes are widely used as photon detectors in the fields of x-ray spectroscopy and electron microscopy.¹ They are also used as electron sources at accelerators because of their many advantages which include high quantum efficiency (QE) and low dark current and their ability to generate electron beams with narrow energy spread and high spin polarization.^{2–4} For electron accelerator applications, considerable effort has been devoted toward improving photocathode QE, electron spin polarization (ESP), and operating lifetime and this work continues today. Photoemission from negative electron affinity (NEA) GaAs photocathodes has been described using Spicer's three-step model (TSM), which considers the mechanisms of photoexcitation, electron transportation, and emission.⁵ Based on this model, an expression for quantum efficiency for GaAs photocathodes was derived by solving the one-dimensional continuity equations.⁶ With the development of numerical simulation techniques, the Monte Carlo (MC) method was used to simulate the electron transportation and emission from GaAs.^{7,8} Recently, the MC method incorporating the TSM was successfully applied to GaAs,⁹ K₂CsSb,¹⁰ and GaN¹¹ photocathodes, predicting the quantum efficiency of these photocathodes in good agreement with experimental data.

To meet some special requirements, thin and ultrathin GaAs photocathodes were manufactured. For example, the thin bulk GaAs and strained-layer GaAs photocathodes were introduced to provide higher electron spin polarization (ESP) than conventional

thick bulk GaAs that typically provides ESP of only ~35%.^{12,13} Spin polarized electrons that diffuse through a thin active layer suffer less depolarization and provide the shortest possible electron bunch length.^{14,15} However, conventional expressions used to predict the quantum efficiency of typical bulk GaAs photocathodes do not accurately predict the experimental data for these photocathodes. Recently, a revised quantum efficiency model for thin GaAs-based photocathodes was proposed by solving the one-dimensional continuity equations based on a three-step model.¹⁶ In this work, we report a Monte Carlo simulation that describes thin GaAs layer grown atop an AlGaAs barrier layer and incorporating photoexcitation, electron transportation in the GaAs, and electron emission at the surface. The simulation was used to explain features of QE spectral response data obtained experimentally and accurately predicts expected behavior, namely, QE is enhanced for thicker GaAs photocathodes and for higher dopant concentrations. More significantly, the simulation predicts that electrons excited to the conduction band (CB) of the GaAs can be reflected by the AlGaAs barrier layer and contribute to enhanced QE. This Monte Carlo model improves our understanding of electron transport within thin GaAs, where the junction interface of the substrate barrier layer must be taken into account.

II. MONTE CARLO MODEL

The MC model was developed incorporating Spicer's TSM depicted schematically in Fig. 1: (1) electrons absorb incident

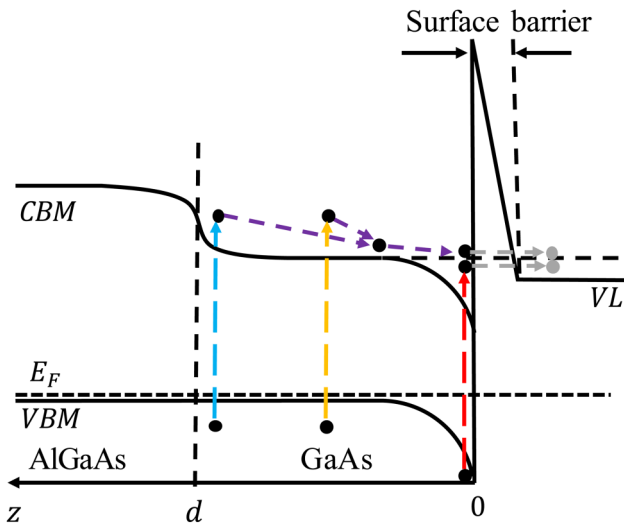


FIG. 1. The energy band diagram of a thin NEA GaAs photocathode grown on an AlGaAs barrier layer, where the vacuum level (VL) lies below the bulk conduction band minimum (CBM). E_F is the Fermi level. The energy bands of GaAs can be divided into three regions: the band bending region (BBR) near the emission surface, the bulk region, and the GaAs-AlGaAs interface region.

photons and are excited from the valence band to the conduction band, (2) these electrons travel to the surface, and (3) finally, the surface electrons cross the surface barrier into the vacuum. In this section, we describe the theories and implementations for each step of photoemission in considerable detail.

Figure 2 shows a flowchart of the MC model. First, the basic parameters of the simulation are specified, such as temperature, dopant, photon energy, and photon number. Then, the initial photoexcited electrons are generated, for which the distributions of energy, momentum, angular, and position are included. The scattering rates for all possible electron scattering mechanisms are then calculated, and these rates depend on the distribution function of the electrons. The electron distributions are calculated and recalculated following scattering at a specified time interval, Δt . Finally, the model evaluates each electron state to see if electrons have recombined with hole, been emitted to vacuum, or survived in the conduction band with continued scattering. The simulation time interval Δt ranged from 2 to 20 fs, which depends on the scattering rate ($\Delta t = 1/5P_{\max}$, with P_{\max} is the maximum scattering rate among all the scattering mechanism at time t). The model runs one cycle at each simulation time interval, and thousands of cycles are required to simulate the electron scattering and emission. The emission process usually finished within 100 ps for thin GaAs samples due to all electrons were emitted into vacuum or recombined back to the valence band (i.e., the number of electrons that stay in the conduction band was zero). Once the emission process finished, the MC simulation stopped. To get convergent results, the incident photon number was set to 100 000.

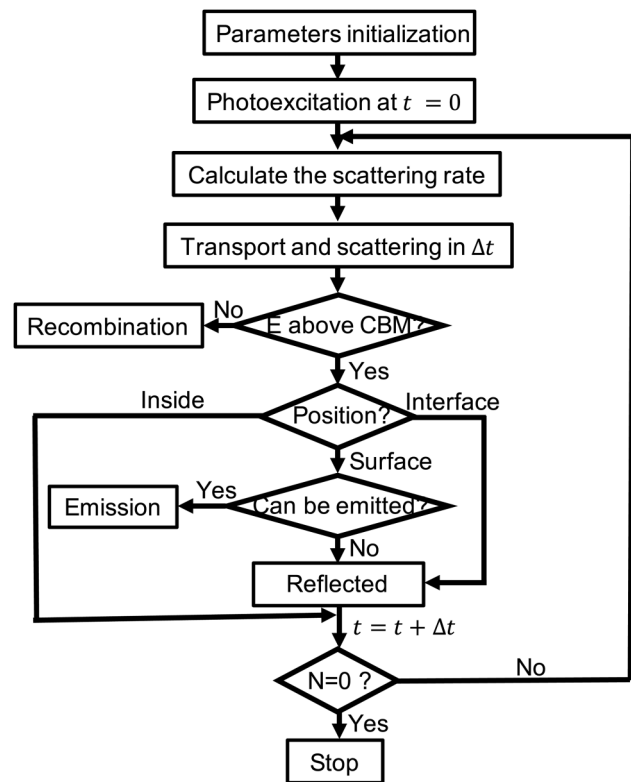


FIG. 2. Flowchart of the Monte Carlo model, where t is the time for excited electrons surviving in the conduction band, Δt is the simulation time interval, and N is the number of excited electrons that still survive in the conduction band after time t .

A. Band structure

The three-valley model⁹ of the first conduction band was used in the MC model. The band structures in the model include the first conduction band and the top three valence bands (heavy hole, light hole, and split-off valence band), where the first conduction band is treated as a combination of three valleys (Γ valley, L valley, and X valley). The top three valence bands are assumed to be parabolic near the Γ point, and the three conduction band valleys are assumed to be nonparabolic. For a nonparabolic band, the dispersion relation is usually treated by means of the Herring-Vogt transformation and given by^{17,18}

$$\gamma_E = E(1 + \alpha_i E) = E_0 + \frac{\hbar^2 |\mathbf{k} - \mathbf{k}_0|^2}{2m_{eff}}, \quad (1)$$

where E_0 and k_0 are the minima energy and wave-vector of the band valleys, respectively, α_i is the nonparabolicity factor for the Γ , L , and X valleys, and m_{eff} is the density of state (DOS) effective mass of electrons in each valley. The parameters used for band structure calculation are listed in Table 1.¹⁹⁻²²

TABLE I. Parameters for conduction and valence bands used in the MC model.

Symbol	Parameters (unit)	Γ	L	X
E_0	Band minima energy (eV)	0	0.29	0.48
m_{eff}	DOS effective mass (m_0)	0.063	0.55	0.85
α	Nonparabolicity factor (1/eV)	0.64	0.461	0.204
Z	Number of equivalent valleys	1	4	3
Φ_d	Acoustic deformation potential (eV)	7.01	9.2	9.0
Symbol	Parameters (unit)	HH	LH	SO
E_0	Band minima energy (eV)	-1.42	-1.42	-1.76
m_{eff}	DOS effective mass (m_0)	0.5	0.076	0.145

B. Photoexcitation

The MC model simulates the reflection-mode photocathode illuminated by a monochromatic light source. The light impinges on the front surface (i.e., the emission surface) of the photocathode and decays exponentially via absorption. The light intensity at a depth z from the surface is given by

$$I = I_0(1 - R)e^{-\alpha_v z}, \quad (2)$$

where I_0 is the intensity of the incident light, R is the surface reflectivity of the material, and α_v is the absorption coefficient of material. The optical constants are calculated using Adachi's model,^{23,24} which provides a good fit to accepted experimental data.¹³ Here, we assume only transitions from any one of the top three valence bands to the Γ , L , and X valleys contribute to the light absorption process. The multiphoton, intervalence band, and higher-order band transitions are ignored because their transition probabilities are very small.

In the photoexcitation process, an electron occupying the energy state E_j in the valence band absorbs a photon $\hbar\omega$ and can be excited to the energy state $E = E_j + \hbar\omega - E_g$, provided there is an empty state with the same energy in the conduction band. The initial energy distribution of the excited electrons in the conduction band can be determined by the convolution of the density of states (DOS) of electrons in the conduction and valence bands.¹⁰ The number $n(E)$ of electrons in the conduction band with energy from E to $E + \Delta E$ is given by

$$n(E) = n_0 \frac{g(E + E_g)g(E + E_g - \hbar\omega)\Delta E}{\int_0^{\hbar\omega - E_g} g(E + E_g)g(E + E_g - \hbar\omega)dE}, \quad (3)$$

where n_0 is the initial photon number, E is the excited electron energy state above the conduction band minimum (CBM), E_g is the bandgap energy, ΔE is the interval energy, and $g(E)$ is the DOS function.²⁵⁻²⁷ The DOS function used in the MC model includes only the top three valence bands and the first conduction band. It is noted that the first conduction band is a continuum in the DOS function, but it is treated as three separated Γ , L , and X valleys in the MC model, which does not affect the energy distribution of the excited electrons because the photon energy considered in the MC model is lower than the energy at the junction between the Γ , L , and X valleys.

Figure 3 shows results from the MC model related to the process of photoexcitation, for illumination with light at 1.8 eV: the position distribution of excited electrons as a function of distance from the photocathode surface and the energy distribution of the excited electrons. The following comments help to appreciate features of the distribution plots. As mentioned above, the energy band diagram of the thin GaAs test samples can be divided into three regions, and each region will have a different energy distribution for electrons excited to the conduction band. In the MC model, the conduction band minimum (CBM) within the bulk region is set to 0 eV; thus, the CBM within the band bending range (BBR) near the emission surface is negative and the CBM at the GaAs-AlGaAs interface region is positive. In the BBR near the surface, the absorption coefficient is considered to

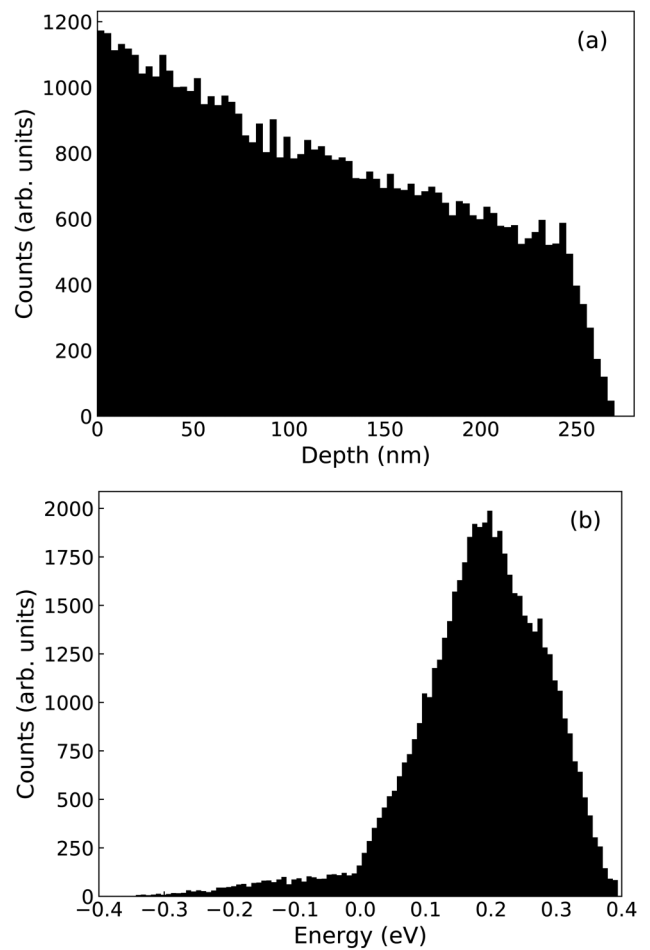


FIG. 3. (a) The position distribution of excited electrons as a function of distance from the photocathode surface and (b) the energy distribution of the excited electrons. These plots were simulated for the GaAs sample with a thickness of 270 nm and a dopant concentration of $8 \times 10^{17} \text{ cm}^{-3}$ when illuminated with 100 000 photons of energy 1.8 eV. The MC model sets the CBM inside the bulk region of the GaAs active layer to 0 eV.

be the same as that in the bulk region, and any other changes caused by the band bending are ignored. Because of these considerations, some electrons excited in the BBR will lie below 0 eV, i.e., their energy is designated negative.

To maintain a constant Fermi level at the vacuum interface, the MC model assumes both valence and conduction bands are bent at the photocathode surface (i.e., this is the nature of the BBR). But at the GaAs-AlGaAs interface region, only the conduction band is bent. This is because the dopant concentration of the AlGaAs layer is only slightly higher than that of GaAs layer, which means the valence band maxima (VBM) of the GaAs and AlGaAs layers are nearly the same. As a result, the photon absorption coefficient will decrease with depth within the GaAs-AlGaAs interface region due to the increasing bandgap. This means electrons excited in this region always lie above 0 eV.

C. Electron transport

Electrons excited to the conduction band will diffuse in all directions with an initial velocity and then experience a variety of scattering processes. The MC model tracks both the real space (position in material) and k-space (momentum and energy) history of the electrons during transportation. A large variety of electron scattering mechanisms in GaAs^{28,29} are shown in Fig. 4. Each scattering process has a different scattering rate, and each process affects real space and k-space behavior in different ways. The physics and implementation of each scattering process included in the MC model is described below.

1. Impurity scattering

There are two types of electron-impurity scattering: neutral impurity and ionized impurity scattering. Typically, neutral impurity scattering can be ignored at room temperature due to the fact that most impurities in GaAs are ionized. Thus, only ionized impurity scattering is considered in this work. Electrons and ionized impurities interact through a screened Coulomb potential, which can be described using the Brooks-Herring (BH) approach. This scattering is treated as an elastic process.

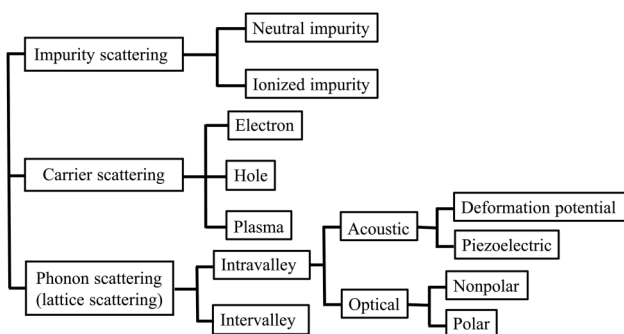


FIG. 4. Electron scattering mechanism in GaAs.

In the BM approach, the screened Coulomb potential is given by³⁰

$$V(r) = \frac{Ze}{4\pi\epsilon_s r} e^{-\beta_s r}, \quad (4)$$

where Z is the number of charge units of ionized impurity, e is the electron charge, ϵ_s is the static dielectric constant of material, r is the distance from the ionized impurity, and β_s is the inverse screening length or inverse screening radius. In the Debye formulation,

$$\beta_s = \sqrt{\frac{n_I e^2}{\epsilon_s k_B T_I}}, \quad (5)$$

in which n_I is the concentration of ionized impurity, k_B is the Boltzmann constant, and T_I is the temperature of the ionized impurity. The ionized impurity scattering rate is given by¹⁸

$$P_{el} = \frac{n_I Z^2 e^4}{32\sqrt{2}\pi\epsilon_s^2 m_{eff}^{\frac{1}{2}} \gamma_E^{\frac{3}{2}}} \frac{b^2}{1+b} \frac{d\gamma_E}{dE}, \quad (6)$$

with

$$b = \frac{4k^2}{\beta_s^2} = \frac{8m_{eff}\gamma_E}{\hbar^2\beta_s^2}, \quad (7)$$

where E is the electron energy, and γ_E is given by Eq. (1).

2. Carrier scattering

Electron-carrier scattering includes electron-electron scattering, electron-hole scattering, and electron-plasma scattering.⁹ The excited electrons may scatter with each other inside the conduction band, and also they may scatter with the electrons in the valence band when their energy is higher than the bandgap E_g .¹⁰ The electron density in GaAs is small and the electron energy considered in this work is smaller than E_g , so electron-electron scattering can be ignored. For p-doped GaAs, the plasma oscillations are heavily damped and any interaction with them can also be ignored.⁷ Thus, only electron-hole scattering is taken into account in the MC model.

As with electron-ionized impurity scattering, electrons and holes interact through a screened Coulomb potential and can be described using the BH approach.³¹ Similarly, the electron-hole scattering rate can be calculated using Eqs. (5) and (6), but replacing quantities related to ionized impurities with the concentration n_h and temperature T_h of holes. Because the hole density is much higher than the electron density, holes can be considered thermalized throughout the simulation, i.e., T_h set to room temperature. Although the electron-hole scattering is elastic, the energy of the electron may change during scattering, resulting in a net transfer of energy from the hot electrons to the thermalized holes until the electron population reaches a steady-state distribution.

3. Phonon scattering

Electron-phonon scattering is the process whereby electrons interact with crystal lattice vibrations. During this process, electrons are scattered from one energy state to another by absorbing or

emitting a phonon. Five varieties of electron-phonon scattering are considered below:

a. Deformation potential (DP) scattering. A deformation potential is a quantity proportional to a matrix element of an operator belonging to a crystal deformation between the final and initial electron state. The interaction of electrons with the crystal lattice through the deformation potential is called DP scattering. This describes the scattering of electrons that results from the crystal strain caused by short-wavelength acoustic waves, and the wave-vectors of the final and initial states of electrons are within the same valley. As such, DP scattering is also called intravalley acoustic deformation potential scattering. The maximum energy transfer (i.e., the acoustic phonon energy) for DP scattering is $2m\nu u_l$, which is much smaller than the electron kinetic energy $m\nu^2/2$, where m is the electron mass, ν is the electron velocity, and u_l is the longitudinal sound velocity. Thus, the DP scattering is considered an elastic scattering process and the scattering rate is given by¹⁸

$$P_{DP} = \frac{\sqrt{2}m_{eff}^{\frac{3}{2}}k_B T_0 \psi_d^2}{\pi \hbar^4 u_l^2 \rho} \gamma_E^{\frac{1}{2}} \frac{d\gamma_E}{dE}, \quad (8)$$

where T_0 is the temperature of material, ψ_d is the acoustic deformation potential, and ρ is the mass density of material.

b. Piezoelectric scattering. Due to the lack of inversion symmetry, a macroscopic electric field is induced in the GaAs crystal lattice known as the piezoelectric effect. This effect provides an additional coupling between electrons and acoustic phonons, and the scattering process is called piezoelectric scattering. This scattering is also assumed to be elastic because the acoustic phonon energy is much smaller than the electron kinetic energy. The scattering rate is given by

$$P_{Pie} = \frac{e^2 K_{av}^2 k_B T_0}{4\pi \epsilon_s \hbar^2 |\nu|} \ln(1 + b), \quad (9)$$

where K_{av}^2 is the electromechanical coupling constant (0.0252 for GaAs),⁹ ν is the electron velocity, and b is given by Eq. (7).

c. Nonpolar optical phonon (NOP) scattering. The phonons that usually dominate in the scattering rate are the long-wavelength optical phonons, which produce a short-range potential within the crystal that shifts the energy states. The modification of energy states per unit ionic displacement associated with optical phonons is called the optical phonon deformation potential, and the interaction of electrons with the crystal lattice through the optical phonon deformation potential is called NOP scattering. The energy associated with nonpolar optical phonons can be assumed to be constant and given by $\hbar\omega_{ij}$ that is comparable to the electron kinetic energy. Thus, the NOP scattering is an inelastic scattering process and the scattering rate for absorption and emission are given by¹⁸

$$P_{NOP} = \frac{Z_{ij} m_{eff}^{\frac{3}{2}} D_{ij}^2}{\sqrt{2} \pi \rho \hbar^3 \omega_{nop}} \left[\frac{N(\omega_{ij})}{N(\omega_{ij}) + 1} \right] \gamma_{E_k'}^{\frac{1}{2}} \frac{d\gamma_{E_k'}}{dE_k'}, \quad (10)$$

where ij means electrons scattering from i valley to j valley, Z_{ij} is the number of equivalent j valleys, D_{ij} is the optical phonon deformation potential, $N(\omega_{ij})$ is the population for nonpolar optical phonon with frequency of ω_{nop} [$N(\omega_{ij})$ is for absorption, $N(\omega_{ij}) + 1$ is for emission], $\gamma_{E_k'}$ is given by Eq. (1), and $E_k' = E_k \pm \hbar\omega_{ij}$ is the final electron energy after scattering, in which k' is the final electron wave-vector.

d. Polar optical phonon (POP) scattering. In polar semiconductors, such as GaAs, long-wavelength optical phonons are also accompanied by a long-range macroscopic electric field which produces additional scattering, called POP scattering. The electron-(longitudinal) polar optical phonon scattering is an important intersubband scattering mechanism for electrons when the intersubband separation is larger than the longitudinal optical phonon energy.³³ The POP scattering rate for absorption and emission is given by^{9,32}

$$P_{POP} = \frac{e^2 \hbar \omega_{pop} \epsilon_p}{4\pi \hbar^2 |\nu|} \left[\frac{N(\omega_{lo})}{N(\omega_{lo}) + 1} \right] \left[\frac{1}{2} \beta_s \left(\frac{1}{\beta_{max}^2 + \beta_s^2} - \frac{1}{\beta_{min}^2 + \beta_s^2} \right) + \ln \left(\frac{\beta_{max}^2 + \beta_s^2}{\beta_{min}^2 + \beta_s^2} \right) \right] \quad (11)$$

with

$$\beta_{min} = \pm \frac{\sqrt{2} m_{eff} \gamma_{E_k}}{\hbar} \left(-1 + \sqrt{1 \pm \frac{\hbar \omega_{lo}}{E_k}} \right), \quad (12)$$

$$\beta_{max} = \frac{\sqrt{2} m_{eff} \gamma_{E_k}}{\hbar} \left(1 + \sqrt{1 \pm \frac{\hbar \omega_{lo}}{E_k}} \right), \quad (13)$$

where $\epsilon_p = \frac{1}{\epsilon_\infty} - \frac{1}{\epsilon_s}$ is the effective dielectric constant of GaAs, ϵ_∞ is the high frequency dielectric constant, $N(\omega_{lo})$ is the population for longitudinal optical phonon with frequency of ω_{lo} , and E_k is the electron energy before scattering. The final electron energy after scattering is given by $E_k' = E_k \pm \hbar\omega_{lo}$.

e. Intervalley scattering. In GaAs, electrons may be scattered by the phonons from one valley to another one, called intervalley scattering. Such scattering is usually treated, formally, in the same way as intravalley scattering by nonpolar optical phonons with a deformation potential interaction.¹⁸ The scattering rate for intervalley scattering is also given by Eq. (10), in which the final electron energy after scattering is changed to $E_k' = E_k \pm \hbar\omega_{ij} - \Delta E_{ij}$. The NOP scattering corresponds to the case $i = j$, and the intervalley scattering corresponds to the case $i \neq j$.

4. Electron tracking

The MC model tracks electron information in 3D space, calculating electron position, velocity, and direction of motion at specified time intervals, Δt , following the many scattering processes. The MC model also tracks energy changes stemming from inelastic scattering. These different scattering processes can be categorized as isotropic or anisotropic. For GaAs, the acoustic phonon and nonpolar optical phonon scattering processes are isotropic, whereas

POP and Coulomb scattering (ionized impurity and hole scattering) are anisotropic processes. The angle θ between the wave-vectors before and after scattering is given by Ref. 34.

For isotropic scattering processes,

$$\cos \theta = 1 - 2r. \tag{14}$$

For anisotropic scattering processes,

$$\cos \theta = \frac{(1 + \xi) - (1 + 2\xi)^r}{\xi}, \tag{15}$$

$$\xi = \frac{2\sqrt{\gamma_{E_k}\gamma_{E_k'}}}{(\sqrt{\gamma_{E_k}} - \sqrt{\gamma_{E_k'}})^2} \text{ (POP)},$$

$$\cos \theta = 1 - \frac{2r}{1 + b(1 - r)} \text{ (Coulomb)}, \tag{16}$$

where r is a random number uniformly distributed between 0 and 1, and b is given by Eq. (7).

Excited electrons obtain energy from the incident light and lose energy by electron-hole scattering and electron-phonon scattering (where impurity scattering is assumed to be elastic and resulting in no energy loss in the MC model). The electron energy relaxation process is illustrated in Fig. 5. The energy of incident light is transferred to electrons. Some electron energy flows to holes by electron-hole scattering, and this energy transfers to the crystal lattice by the hole-phonon scattering. And, some electron energy flows directly to the crystal lattice by electron-phonon scattering. During electron-phonon scattering, the electron also obtains energy from the crystal lattice by absorption of phonons. Electrons will reach a steady-state distribution after experiencing a series of scattering events.

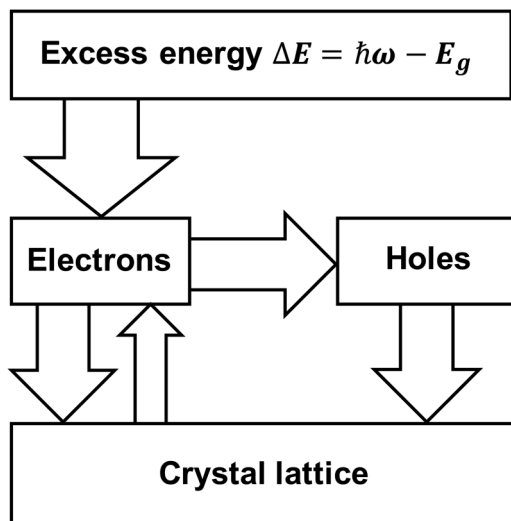


FIG. 5. The energy-flow channels in GaAs with incident photon energy, the width of the arrows indicates the relative size of each energy-flow channel.

5. Band bending considerations

The downward sloping conduction band at the GaAs-AlGaAs interface and in the BBR can strongly influence electron transport within the photocathode. A bent conduction band serves to provide an internal electric field that can change the kinetic energy of the electrons. Electrons in these regions can gain energy and be rapidly propelled toward the emission surface under the influence of the internal electric field or have their trajectories modified via reflection. The MC model treated the GaAs-AlGaAs interface and the BBR as triangle shape with widths of 7–38 nm, which depend on the dopant concentration of the photocathode.⁹ The MC model accounts for electron transport features related to the conduction band bending at the GaAs-AlGaAs interface region and in the BBR near the emission surface.

Electrons in the GaAs-AlGaAs interface region and bulk region with total energy below the CBM will be trapped and returned to the valence band. And, electrons in the BBR with total energy below vacuum level will be trapped and eventually will be captured by a surface state. From these states, they can come back to the bulk valence band.

To verify the accuracy of the MC model as it relates to electron transport in the conduction band, MC simulation results were compared to predictions based on the conventional diffusion equation,^{6,13} for electron transport in very thick p-type bulk GaAs. In the model, the bulk region thickness was set to 10 μm, which is much larger than the laser absorption length of ~2 μm. The number of electrons that reach the surface was obtained by the MC simulation, and then the transport efficiency was calculated by dividing the surface electron number by the total number of electrons excited to the conduction band. The results of this comparison are shown in Fig. 6. When only the bulk region was considered, the transport efficiency agrees with the conventional diffusion equation. But when the band bending of the conduction band is considered, the transport efficiency is larger, which speaks to the significance of the internal electric field in the BBR.

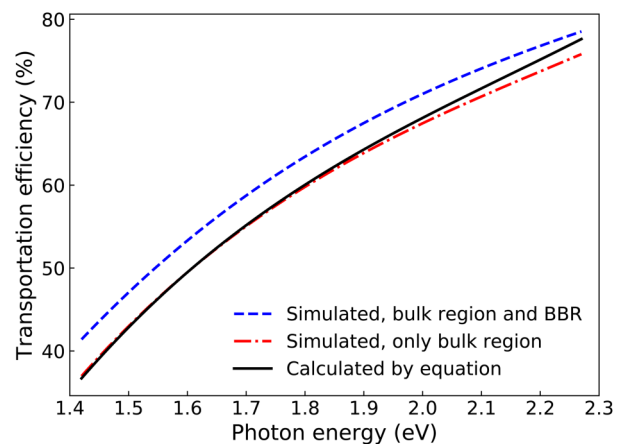


FIG. 6. Transport efficiency of electrons in the conduction band for very thick p-type bulk GaAs with a dopant concentration of $1 \times 10^{19} \text{ cm}^{-3}$. When the BBR region is accounted for in the MC model, transport efficiency to the photocathode surface is enhanced.

D. Emission

As mentioned above, when electrons reach the surface, they can either be reflected backward by the surface barrier or cross the barrier into vacuum. Electrons that cross the surface barrier into vacuum must overcome the barrier or tunnel through it. The exact parameters of the surface barrier depend significantly on the photocathode surface preparation and activation procedure and are critical to calculating the emission probability. In the literature, rectangular³⁵ and triangular³⁶ barriers have been modeled by fitting quantum efficiency and energy distributions of emitted electrons, respectively. In our MC model, the triangular barrier was used to calculate the electron transmission probability and assigned a height of 4 eV and a width of 1.5 Å, as shown in Fig. 7.

The transmission probability across the surface barrier was calculated using the transfer matrix (TM) method^{37,38} which solves the Schrodinger equation for electrons across an arbitrary potential by dividing the potential into series of stair-step rectangular potentials. Figure 7 shows the triangular surface barrier used in the MC model consisting of 10 rectangular potentials, but 100 rectangular potentials were used in the MC model. The transmission probability was calculated by $T = \frac{1}{|P_{11}|^2}$, where P is the transfer matrix for the surface barrier and given by $P = \prod_{j=1}^N P_j$, in which P_j is a 2×2 matrix calculated from the Schrodinger equation in j th rectangular potential region with length L_j ,³⁷

$$P_j = P_{j,free}P_{j,step} = \frac{1}{2\sqrt{k_{j,\parallel}k_{j+1,\parallel}}} \times \begin{bmatrix} (k_{j,\parallel} + k_{j+1,\parallel})e^{-ik_{j,\parallel}L_j} & (k_{j,\parallel} - k_{j+1,\parallel})e^{-ik_{j,\parallel}L_j} \\ (k_{j,\parallel} - k_{j+1,\parallel})e^{ik_{j,\parallel}L_j} & (k_{j,\parallel} + k_{j+1,\parallel})e^{ik_{j,\parallel}L_j} \end{bmatrix}, \quad (17)$$

where $P_{j,free}$ is the transfer matrix for electrons propagating in the j th rectangular potential region, $P_{j,step}$ is the transfer matrix for electrons

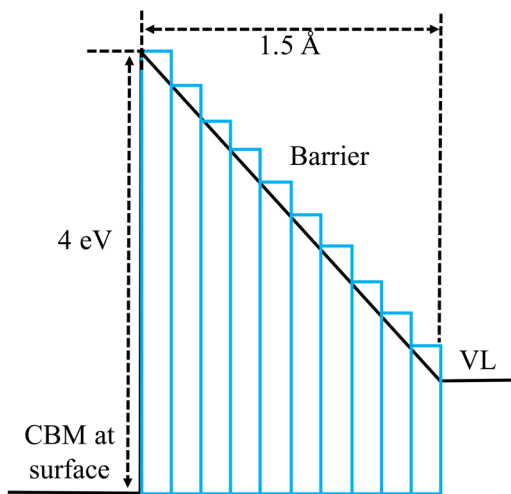


FIG. 7. The photocathode surface barrier, shown approximated by a series of stair-step rectangular potentials, used to calculate the transmission probability via the transfer matrix (TM) method.

propagating from j th rectangular potential region to $(j + 1)$ th rectangular potential region, and $k_{j,\parallel}$ is the electron longitudinal wave-vector in j th rectangular potential region. The conservation of electron energy and transverse momentum should be obeyed when electrons cross the potential barrier, resulting in $E_j = E_{j-1} - \Delta E_{j,j-1} = E - V_j$ and $k_{j,\perp} = k_{j-1,\perp} = k_{\perp} + \Lambda_{\perp}$. Thus, the $k_{j,\parallel}$ term is given by

$$k_{j,\parallel} = \frac{1}{\hbar} \sqrt{2m_j(E - V_j) - (\hbar k_{\perp} + \hbar \Lambda_{\perp})^2}, \quad (18)$$

where E and k_{\perp} are, respectively, the total kinetic energy and transverse wave-vector of electrons above the valley bottom at the surface in which they attempt to cross the surface barrier. The term Λ_{\perp} is the transverse wave-vector of electrons corresponding to the valley bottom. The terms V_j and m_j are the potential and the effective mass of electrons in j th rectangular potential region, respectively. In the MC model, electrons are assumed to be in vacuum when they move into the barrier, i.e., the effective mass of the electron changes instantaneously to vacuum mass at the interface of GaAs ($j = 0$) and the first rectangular potential region ($j = 1$). Thus, $m_0 = m_{eff}$ and $m_j = m_e$ for $j > 0$. It is worth mentioning that the $k_{0,\parallel}/k_{1,\parallel}$ in Eq. (18) should be replaced with $m_e k_{0,\parallel}/m_{eff} k_{1,\parallel}$ to satisfy the continuity of the Schrodinger equation. m_{eff} can be equal to either m_{Γ} , m_L , or m_X , depending on which conduction valley the electrons are located when they cross the barrier and the direction of the surface normal. For example, only electrons in Γ valley and certain X valley are allowed to emit from the (100) surface.^{9,36} The transmission probability of electrons through the surface barrier from the Γ valley as a function of the longitudinal kinetic energy is shown in Fig. 8. The difference between the effective mass of the electron in GaAs and vacuum ($m_{eff} < m_e$) will cause a refraction that narrows the escape angle around the surface normal. For Γ valley electrons with NEA surface, the calculated escape angle is less than 15°, which has been observed experimentally.³⁹

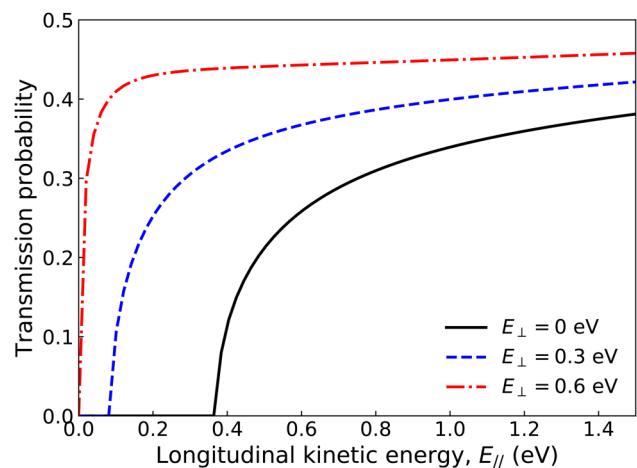


FIG. 8. The transmission probability of electrons through the GaAs surface barrier, calculated for electrons in the valley with a dopant concentration of $8 \times 10^{17} \text{ cm}^{-3}$ and an electron affinity (E_A) of -0.04 eV .

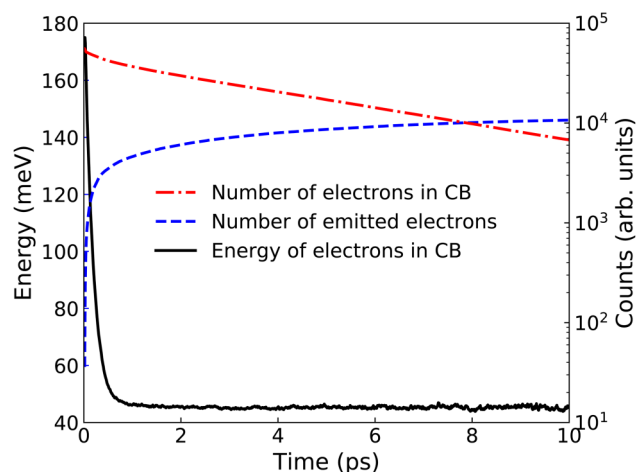


FIG. 9. Time evolution of the number of electrons in the conduction band (CB) emitted to vacuum, and the energy of electrons in the conduction band (CB) simulated for a GaAs photocathode with a thickness of 270 nm, a dopant concentration of $8 \times 10^{17} \text{ cm}^{-3}$, and an electron affinity of -0.04 eV , for illumination by 100 000 photons of energy 1.8 eV.

The time evolution of the number of excited and emitted electrons is shown in Fig. 9, for a 270 nm thick GaAs photocathode with a dopant concentration of $8 \times 10^{17} \text{ cm}^{-3}$ and an electron affinity of -0.04 eV . (The reason for choosing electron affinity -0.04 eV is discussed below.) The simulation predicts $\sim 56\,000$ electrons will be excited to the conduction band when illuminated by 10^5 photons with 1.8 eV photon energy. Electrons diffuse to the surface and those with sufficient energy are quickly emitted. Approximately 40% of the electrons that reach the emission surface are emitted, and this occurs very quickly, in less than 1 ps (blue curve). The average energy of the excited electrons in the conduction band quickly falls due to scattering processes (black curve). And beyond 1 ps, emission continues but at a lower rate. The total number of excited electrons that stay in the conduction band (called “electrons in the conduction band” in Fig. 9) falls steadily as electrons leave the conduction band (red curve), but photoemission essentially stops after approximately 40 ps (note only a 10 ps time window is shown in Fig. 9).

Figure 10 shows the two-dimensional (2D) distribution of emitted and excited electrons for a 270 nm thick GaAs photocathode with a dopant concentration of $8 \times 10^{17} \text{ cm}^{-3}$ and an electron affinity of -0.04 eV and for a Gaussian laser spatial distribution with $\sigma = 0.25 \text{ mm}$ and 1.8 eV photon energy. The electron distributions mimic that of the laser profile as a result of scattering in the material and because the electrons are emitted very quickly, so there is very little opportunity for the electrons to diffuse far from the initial laser distribution and still escape to vacuum.

III. EXPERIMENT AND QE SPECTRAL RESPONSE RESULTS

The experimental assessment of photocathode QE was performed at Jefferson Lab. Five GaAs samples with varying active layer

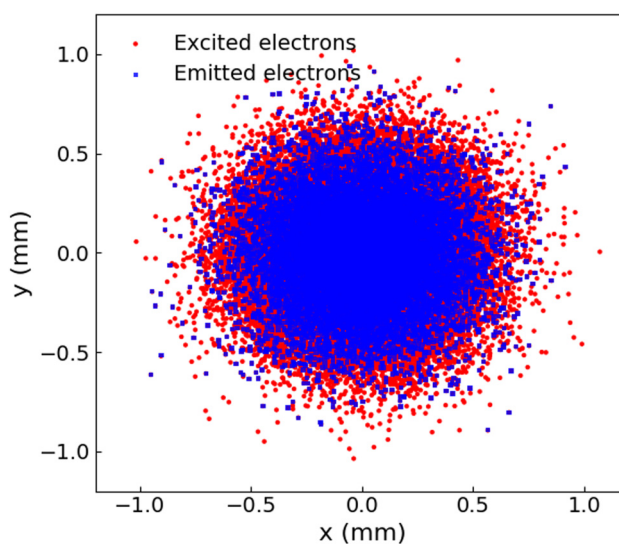


FIG. 10. The 2D distribution of excited and emitted electrons simulated for a GaAs photocathode with a thickness of 270 nm, a dopant concentration of $8 \times 10^{17} \text{ cm}^{-3}$, and an electron affinity of -0.04 eV under excitation with 1.8 eV photons. The laser was assigned a Gaussian spatial distribution with $\sigma = 0.25 \text{ mm}$.

thickness and dopant density were purchased from a commercial vendor.⁴⁰ The samples were fabricated on 2 in. diameter p-type GaAs substrates using the process of metal-organic chemical vapor deposition (MOCVD) and composed of a 200 nm p-type GaAs buffer layer, a $\sim 900 \text{ nm}$ $\text{Al}_{0.3}\text{Ga}_{0.7}\text{As}$ barrier layer, and the GaAs active layer of interest, with specifications detailed in Table II. Because GaAs and AlGaAs have very nearly identical lattice constants, the ternary alloy barrier layer can be grown on GaAs without introducing significant strain. One at a time, samples were installed within a vacuum chamber (Fig. 11) that was pumped by nonevaporable getter and ion pumps and baked at $250 \text{ }^\circ\text{C}$ for approximately 36 h inside a hot-air oven. Following bake-out, the vacuum chamber routinely achieved 10^{-11} Torr-scale pressure.

Photocathode samples were attached to a molybdenum plug using indium foil and a retaining ring made of tantalum. The molybdenum plug was brazed to the end of a stainless-steel tube, into which a heater could be inserted, and providing a means to heat samples via thermal conduction. Samples were heated to $\sim 575 \text{ }^\circ\text{C}$ for 2 h and cooled to room temperature and then “activated” to achieve a negative electron affinity condition by applying Cs and NF_3 using a yo-yo activation protocol. At this point, the relative QE spectral response was measured using a white light monochromator which produced wavelength-tunable light with a spatial profile that exceeded the size of the photocathode. Accurate QE values were assigned by scaling the monochromator data to an exact QE value obtained at 770 nm using a low power diode laser that illuminated only a small region of the photocathode.

Samples were cut to size using different techniques: simple cleaving into $15 \times 15 \text{ mm}$ squares or using a stainless-steel cup-shaped cutting tool with a diamond-grit slurry to provide 15 mm

TABLE II. The parameters of five photocathode samples.

Sample	1	2	3	4	5
p-type GaAs active layer					
Thickness (nm)	140	180	180	270	270
Dopant concentration (cm^{-3})	3.8×10^{17}	9.0×10^{17}	3.7×10^{18}	5.8×10^{17}	8.0×10^{17}
p-type $\text{Al}_{0.3}\text{GaAs}$ barrier layer					
Thickness (nm)	900	960	870	940	950
Dopant concentration (cm^{-3})	4.3×10^{17}	1.0×10^{18}	3.7×10^{18}	6.0×10^{17}	9.5×10^{17}

diameter disks. When using the second method, a protective microscope cover slide was affixed to the surface of the sample using an acetone-soluble wax. Because handling the photocathode can introduce contamination on the surface, particularly when using the cutting method involving wax and diamond-slurry abrasive, samples were subjected to repeated intervals of *in situ* atomic-hydrogen cleaning as described in Refs. 41 and 42. Following each exposure to atomic hydrogen, samples were heated, cooled, and reactivated, and the QE spectral response was re-evaluated. Hydrogen cleaning was repeated until QE values were essentially unchanged following

successive activations. The results presented in Fig. 12 show the highest QE values obtained from each sample. Spectral response curves exhibit the expected trend, with QE falling to small values as photon energy approaches the bandgap energy. Thicker GaAs samples and higher dopant densities provided the highest QE, and this is reasonable. A thicker active layer can absorb more photons, which means more electrons can be excited into the conduction band, thus more electrons reach the surface to be emitted. And a higher dopant concentration serves to increase band bending which helps to drive electrons toward the emission surface, and it also reduces the surface work function, both factors leading to higher QE.

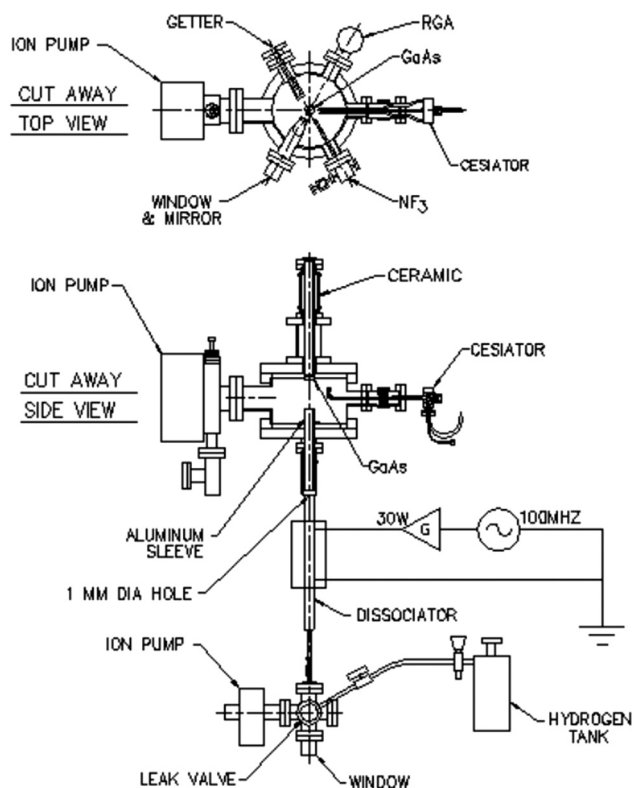


FIG. 11. Schematic diagram of the vacuum chamber used to evaluate the photocathode QE spectral response of the five GaAs photocathodes. The vacuum chamber included an atomic-hydrogen dissociator for *in situ* atomic-hydrogen cleaning of each sample.

IV. COMPARING MC MODEL PREDICTIONS AND EXPERIMENTAL RESULTS

The electron affinity (i.e., the surface work function) is a very important but complicated parameter because it is influenced by many factors, such as the dopant concentration and surface contamination that is sometimes unknown and hard to control. By evaluating the thin GaAs samples that form the basis of this study in the same vacuum apparatus and using the same methodology, and

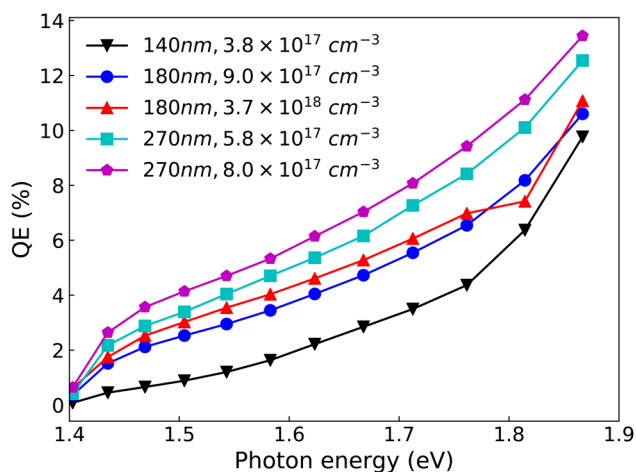


FIG. 12. The experimental spectral response curves for the five GaAs photocathode samples, with information about active layer thickness and dopant concentration provided in the legend. The unsmooth of red line above 1.8 eV caused by the experimental system error.

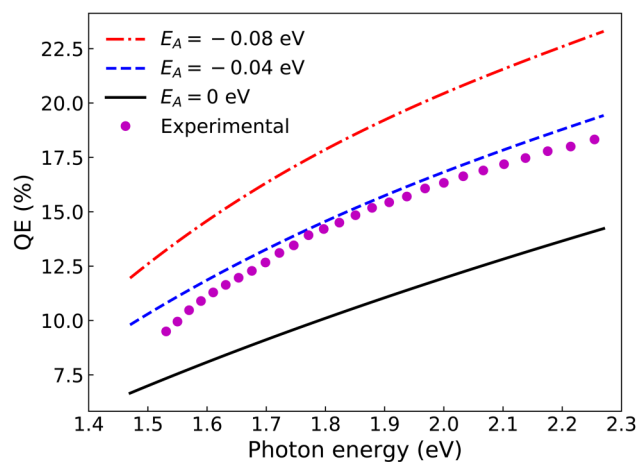


FIG. 13. To assign a value to electron affinity (E_A), simulation results were compared to actual QE measurements from thick bulk GaAs with a dopant concentration of $1 \times 10^{19} \text{ cm}^{-3}$. The best fit to experimental results was obtained for $E_A = -0.04 \text{ eV}$.

repeatedly cleaning the sample with atomic hydrogen, uncertainty associated with surface contamination was minimized. But because the samples have different dopant concentrations, the electron affinity was not expected to be constant. To assign a reasonable value to electron affinity, the MC model was used to predict QE as a function of photon energy (i.e., the QE spectral response) for thick bulk GaAs (thickness set to $10 \mu\text{m}$), for which electron reflection at the buffer layer is not relevant. Figure 13 shows the simulated spectral response obtained for various electron affinity values and compared to experimental results¹³ for bulk p-type GaAs with dopant concentration $1 \times 10^{19} \text{ cm}^{-3}$. The best match between the simulated and experimental results was obtained for electron affinity -0.04 eV . Based on this result, for the thin GaAs photocathode samples, the MC model used electron affinity as a variable set to values within the range of -0.05 to -0.03 eV , to obtain the best fit between experimental and simulated results.

Predicted QE spectral response curves for two of the thin GaAs samples described in Table II are shown in Fig. 14, together with experimental measurements first presented in Fig. 12. For clarity, only the results for two samples are displayed, but similar plots were obtained for all five samples. There is good agreement between measurement and prediction for photon energies below $\sim 1.65 \text{ eV}$ [see Fig. 14(a)]. As mentioned above, the MC model simulated only the electrons produced in the GaAs active layer and not electrons produced in the AlGaAs barrier layer. It must be noted that the bandgap of $\text{Al}_{0.3}\text{GaAs}$ is 1.8 eV .⁴³ When photon energy exceeds $\sim 1.8 \text{ eV}$, the AlGaAs barrier layer begins to absorb light, sending additional electrons to the conduction band and some of these electrons escape to vacuum thereby enhancing QE. More precisely, the AlGaAs barrier layer also absorbs photons with energy lower than 1.8 eV because of the depletion layer at the AlGaAs/GaAs interface, which was not considered in the MC model. Thus, the best agreement between predicted and measured

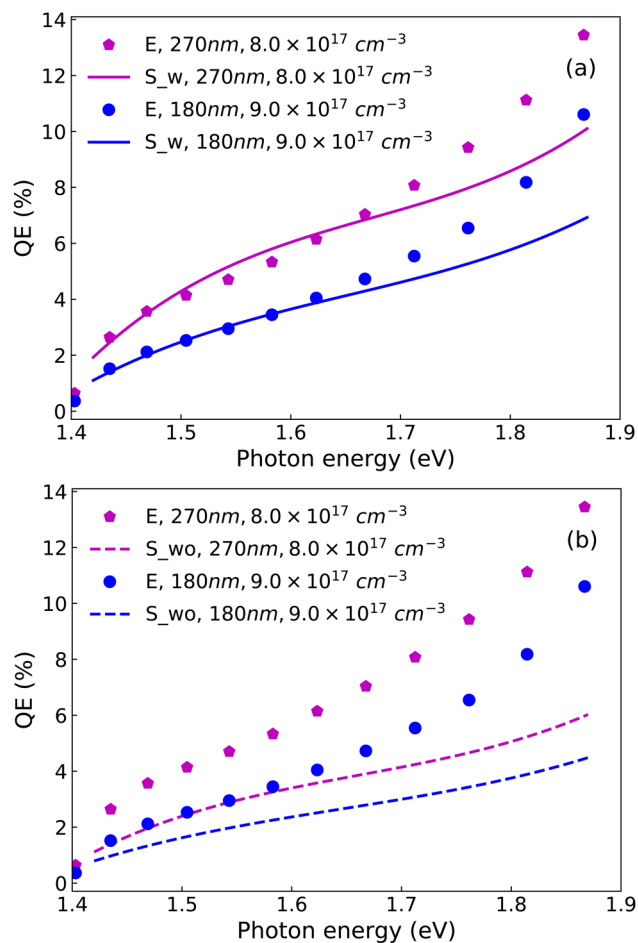


FIG. 14. Comparison of simulated (S) and experimental (E) spectral response for two photocathode samples labeled 2 and 5 in Table II (a) for the full MC model that included reflections at the AlGaAs/GaAs interface and (b) for the reflection at the AlGaAs/GaAs interface not included. Electron affinity was set to -0.04 eV and -0.05 eV , respectively.

QE values occurs for lower photon energies. The importance of considering reflection at the AlGaAs/GaAs interface is abundantly clear as shown in Fig. 14(b), where there is marked disagreement between predicted and measured QE, when reflected electrons are ignored in the simulation.

V. TEMPORAL RESPONSE

Besides predicting photocathode QE spectral response, the MC model was used to evaluate the temporal pulse-response times of the different photocathodes, although experimental measurements were not performed at Jefferson Lab. The “pulse-response time” τ_{90} is defined as the time interval in which 90% of the pulse charge is contained. When illuminated with 1.8 eV photon energy, the MC model predicts electron response pulse-response times ranging

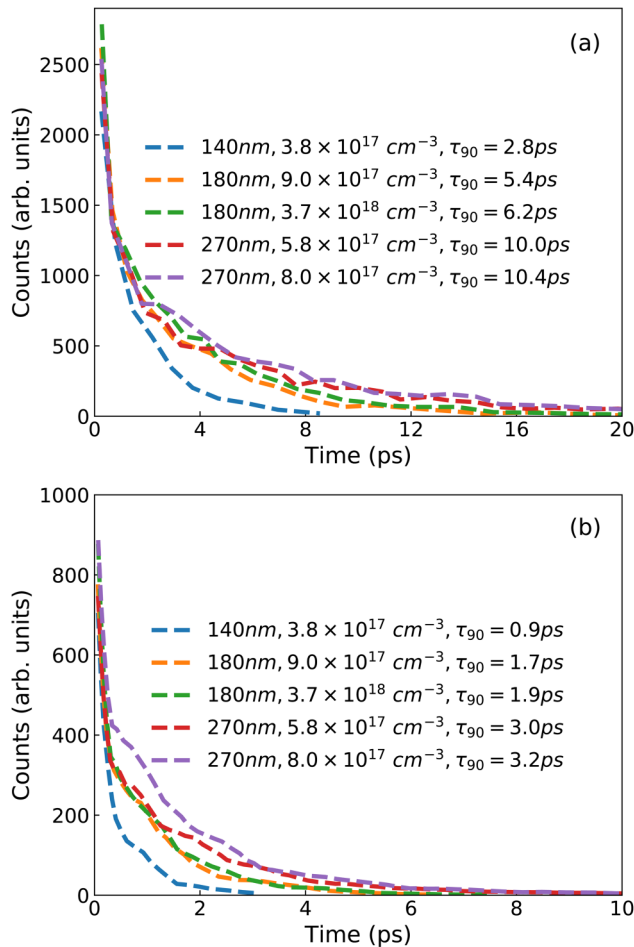


FIG. 15. The simulated temporal response curves of five photocathode samples under 1.8 eV photon excitation (a) for the full MC model that included reflections at the AlGaAs/GaAs interface, and (b) when reflection at the AlGaAs/GaAs interface was not included. The “pulse-response time” τ_{90} is defined as the interval in which the 90% of the pulse charge is contained.

from 3 to 10 ps, with thicker samples providing longer bunches, as expected (see Fig. 15). Although the stated τ_{90} values are very small, the MC predictions show very long tails that extend many tens of picoseconds beyond the central bunch, for each of the photocathode samples, a phenomenon observed experimentally.^{44,45} Much shorter pulses are predicted when electron reflection at the AlGaAs/GaAs interface is ignored, with τ_{90} predictions ranging from 1 to 3 ps (see Fig. 15), but by now it should be obvious to the reader that reflections cannot be ignored. Less obvious is the observation that higher dopant density also serves to increase the length of emitted bunches. Higher dopant density leads to higher hole density, and consequently resulting in an increased electron scattering rate. Thus, electrons in conduction band will suffer more scattering for GaAs samples with higher dopant concentration, resulting in longer response time. What is

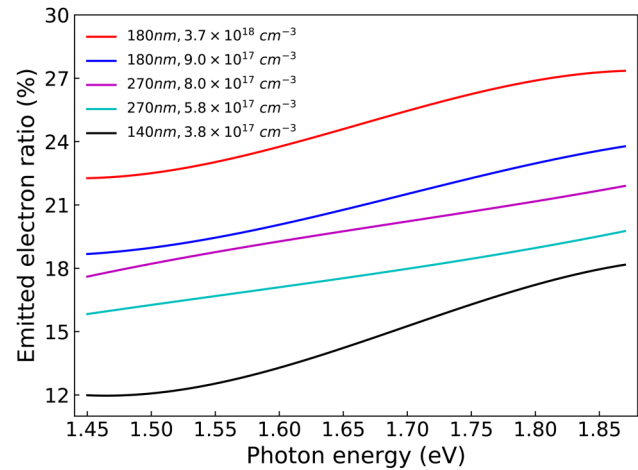


FIG. 16. The simulated ratio of emitted electrons to excited electrons for five samples. The NEA for all samples are set to -0.04 eV . Higher dopant concentration exhibits higher emission probability.

more, lower dopant density leads to a weaker band bending, and consequently resulting in a higher electron affinity, which can filter out the low energy electrons, as a result of shorter response time.

The MC predictions described here are in agreement with measurements reported in the literature.^{14,45,46} In particular, the group at the University of Mainz has performed extensive temporal response studies of unstrained and strained GaAs, as a function of active layer thickness, dopant density, and laser illumination wavelength. For example, Aulenbacher *et al.* measured a response time of 4.6 ps from a thin GaAs photocathode with a 200 nm active layer,⁴⁷ comparable to the predicted response time of 5.4 ps from the thin GaAs sample described here that was 180 nm thick.

In the references mentioned above, temporal response measurements were compared to predictions based on a one-dimensional diffusion model, which provided very good fits to experimental data; however, in light of discussions presented here noting the inadequacy of the diffusion model to adequately predict reflection at the band bending regions, it seems likely that good fits to data might simply be a result of using the diffusion coefficient as a fit parameter. This assertion is supported by noting that diffusion coefficient values obtained from fitting were not in total agreement with the published values.^{45,46}

VI. DISCUSSION AND CONCLUSION

A final analysis of the five thin photocathode samples is shown in Fig. 16, which presents the ratio of emitted electrons to excited electrons, a metric termed the “emitted electron ratio.” The MC model makes clear the impact of active layer thickness and dopant concentration as important factors that affect the spectral response of GaAs photocathodes. A thicker GaAs active layer absorbs more light and produces more excited electrons, which results in higher QE. On the other hand, electrons within thick photocathode layers suffer more scattering, which leads to energy loss before reaching the

emission surface which will decrease the emission probability; however, the MC model shows this effect to be relatively small. Rather, it is the dopant concentration that predominantly dictates emission. Higher dopant concentration deeper the band bending region and lower the vacuum level, which helps to increase the emission probability and leads to higher QE. One can see from the figure that the dopant concentration dominates the emission probability.

This work presents a Monte Carlo simulation based on the three-step model describing photoemission from thin GaAs photocathodes that accurately predicts experimental results. The thin GaAs photocathodes were modeled as three regions: the interface region between GaAs and barrier layer, the bulk region, and the band bending region. Electron production and transport is different in each region as a result of scattering processes and internal electric fields which significantly impact electron transport to the surface.

This study helps to improve our understanding of the evolution of electrons in thin GaAs photocathodes and should permit optimization of desired photoemission characteristics. The Monte Carlo simulation is a powerful technique to study the physical processes of photoemission. We believe our simulation can be applied to other III-V semiconductors and can also be extended to more complicated multilayer structures.

ACKNOWLEDGMENTS

We thank Dr. Matthew Poelker and Dr. Charles Sinclair from Jefferson Lab for providing the experimental data and for useful discussions related to the experimental work and theoretical analysis. We thank Dr. Dimitre Dimitrov for useful discussions related to how to deal with photoexcitation, band structure, and the surface barrier. This work was performed at the Brookhaven National Laboratory and authored by Brookhaven Science Associates, LLC under Contract No. DE-SC0012704, with the U.S. DOE. The U.S. Government retains a nonexclusive, paid-up, irrevocable, world-wide license to publish or reproduce this manuscript for U.S. Government purposes.

REFERENCES

- ¹G. Lioliou and A. M. Barnett, *Nucl. Instrum. Methods Phys. Res. Sect. A* **836**, 37 (2016).
- ²S. Karkare, L. Boulet, L. Cultrera, B. Dunham, X. Liu, W. Schaff, and I. Bazarov, *Phys. Rev. Lett.* **112**, 097601 (2014).
- ³W. Liu, Y. Chen, W. Lu, A. Moy, M. Poelker, M. Stutzman, and S. Zhang, *Appl. Phys. Lett.* **109**, 252104 (2016).
- ⁴B. Dunham, J. Barley, A. Bartnik, I. Bazarov, L. Cultrera, J. Dobbins, G. Hoffstaetter, B. Johnson, R. Kaplan, S. Karkare *et al.*, *Appl. Phys. Lett.* **102**, 10 (2013).
- ⁵W. E. Spicer, *Phys. Rev.* **112**, 114 (1958).
- ⁶W. E. Spicer and A. Herrera-Gomez, *Proc. SPIE* **2022**, 18 (1993).
- ⁷H. Taniyama, M. Tomizawa, T. Furuta, and A. Yoshii, *J. Appl. Phys.* **68**, 621 (1990).
- ⁸G. Vergara, A. Herrera-Gómez, and W. E. Spicer, *J. Appl. Phys.* **80**, 1809 (1996).
- ⁹S. Karkare, D. Dimitrov, W. Schaff, L. Cultrera, A. Bartnik, X. Liu, E. Sawyer, T. Esposito, and I. Bazarov, *J. Appl. Phys.* **113**, 104904 (2013).
- ¹⁰H. Xie, I. Ben-Zvi, T. Rao, T. Xin, and E. Wang, *Phys. Rev. Accel. Beams* **19**, 1 (2016).
- ¹¹J. Marini, L. D. Bell, and F. Shahedipour-Sandvik, *J. Appl. Phys.* **123**, 124502 (2018).
- ¹²G. Fishman and G. Lampel, *Phys. Rev. B* **16**, 820 (1977).
- ¹³W. Liu, M. Poelker, X. Peng, S. Zhang, and M. Stutzman, *J. Appl. Phys.* **122**, 035703 (2017).
- ¹⁴P. Hartmann, J. Bermuth, J. Hoffmann, S. Köbis, E. Reichert, H. G. Andresen, K. Aulenbacher, P. Drescher, H. Euteneuer, H. Fischer *et al.*, *Nucl. Instrum. Methods Phys. Res. Sect. A* **379**, 15 (1996).
- ¹⁵P. Hartmann, "Aufbau Einer Gepulsten Quelle Polarisiert Elektronen," Ph.D. dissertation (Shaker Verlag, Aachen, 1998), ISBN: 3-8265-3411-5.
- ¹⁶C. Feng, Y. Zhang, Y. Qian, F. Shi, J. Zou, and Y. Zeng, *J. Appl. Phys.* **117**, 023103 (2015).
- ¹⁷C. Herring and E. Vogt, *Phys. Rev.* **101**, 944 (1956).
- ¹⁸C. Jacoboni and L. Reggiani, *Rev. Mod. Phys.* **55**, 645 (1983).
- ¹⁹J. S. Blakemore, *J. Appl. Phys.* **53**, R123 (1982).
- ²⁰See <http://www.matprop.ru/GaAs> for "Physical Properties of GaAs."
- ²¹M. Levinstein, S. Rumyantsev, and M. Shur, *Handbook Series on Semiconductor Parameters* (World Scientific, 1999).
- ²²M. Lundstrom, *Fundamentals of Carrier Transport* (Cambridge University Press, 2000).
- ²³S. Adachi, *J. Appl. Phys.* **53**, 5863 (1982).
- ²⁴S. Adachi, *J. Appl. Phys.* **58**, R1 (1985).
- ²⁵Y. P. Tan, M. Povolotskiy, T. Kubis, T. B. Boykin, and G. Klimeck, *Phys. Rev. B* **92**, 085301 (2015).
- ²⁶M. L. Cohen and J. R. Chelikowsky, *Electronic Structure and Optical Properties of Semiconductors* (Springer-Verlag, 1989).
- ²⁷See <https://materialsproject.org> for more information about The Materials Project.
- ²⁸R. K. Ahrenkiel and M. S. Lundstrom, *Minority Carriers in III-V Semiconductors Physics and Applications* (Academic Press, Inc., 1993).
- ²⁹S. Adachi, *Properties of Group-IV, III-V and II-VI Semiconductors* (John Wiley & Sons Ltd, 2005).
- ³⁰D. Chattopadhyay and H. J. Queisser, *Rev. Mod. Phys.* **53**, 745 (1981).
- ³¹M. A. Osman and D. K. Ferry, *Phys. Rev. B* **36**, 6018 (1987).
- ³²B. K. Ridley, *Quantum Processes in Semiconductors* (Oxford University Press, 2013).
- ³³M. Hartig, S. Haacke, B. Deveaud, and L. Rota, *Phys. Rev. B* **54**, R14269 (1996).
- ³⁴D. Vasileska and S. M. Goodnick, see <https://nanohub.org/resources/9109> for "Bulk Monte Carlo: Implementation Details and Source."
- ³⁵D. G. Fisher, R. E. Enstrom, J. S. Escher, and B. F. Williams, *J. Appl. Phys.* **43**, 3815 (1972).
- ³⁶G. Vergara, A. Herrera-Gómez, and W. E. Spicer, *Surf. Sci.* **436**, 83 (1999).
- ³⁷A. F. J. Levi, *Applied Quantum Mechanics* (Cambridge University Press, 2003).
- ³⁸G. P. Gilfoyle, *Comput. Phys. Commun.* **121**, 573 (1999).
- ³⁹Z. Liu, Y. Sun, P. Pianetta, and R. F. W. Pease, *J. Vac. Sci. Technol. B* **23**, 2758 (2005).
- ⁴⁰See <http://www.bandwidthsemi.com> for "Spire Semiconductor LLC."
- ⁴¹C. K. Sinclair, B. M. Poelker, and J. S. Price, in *Proceedings of the 1997 Particle Accelerator Conference* (IEEE, 1997), pp. 2864–2866.
- ⁴²M. Baylac, P. Adderley, J. Brittan, J. Clark, T. Day, J. Games, J. Hansknecht, M. Poelker, M. Stutzman, A. T. Wu, and A. S. Terekhov, *Phys. Rev. ST Accel. Beams* **8**, 123501 (2005).
- ⁴³M. El Allali, C. B. Sorensen, E. Veje, and P. Tidemand-Petersson, *Phys. Rev. B* **48**, 4398 (1993).
- ⁴⁴M. A. Dehn, K. Aulenbacher, V. Bechthold, and F. Fichtner, *Appl. Phys. Lett.* **111**, 132105 (2017).
- ⁴⁵I. V. Bazarov, B. M. Dunham, Y. Li, X. Liu, D. G. Ouzounov, C. K. Sinclair, F. Hannon, and T. Miyajima, *J. Appl. Phys.* **103**, 054901 (2008).
- ⁴⁶P. Hartmann, J. Bermuth, D. V. Harrach, J. Hoffmann, S. Köbis, E. Reichert, K. Aulenbacher, J. Schuler, and M. Steigerwald, *J. Appl. Phys.* **86**, 2245 (1999).
- ⁴⁷K. Aulenbacher, J. Schuler, D. V. Harrach, E. Reichert, J. Röhthgen, A. Subashev, V. Tioukine, and Y. Yashin, *J. Appl. Phys.* **92**, 7536 (2002).